Volume 17
Number 46
14 December 2025
Pages 26463-27026

Nanoscale

rsc.li/nanoscale

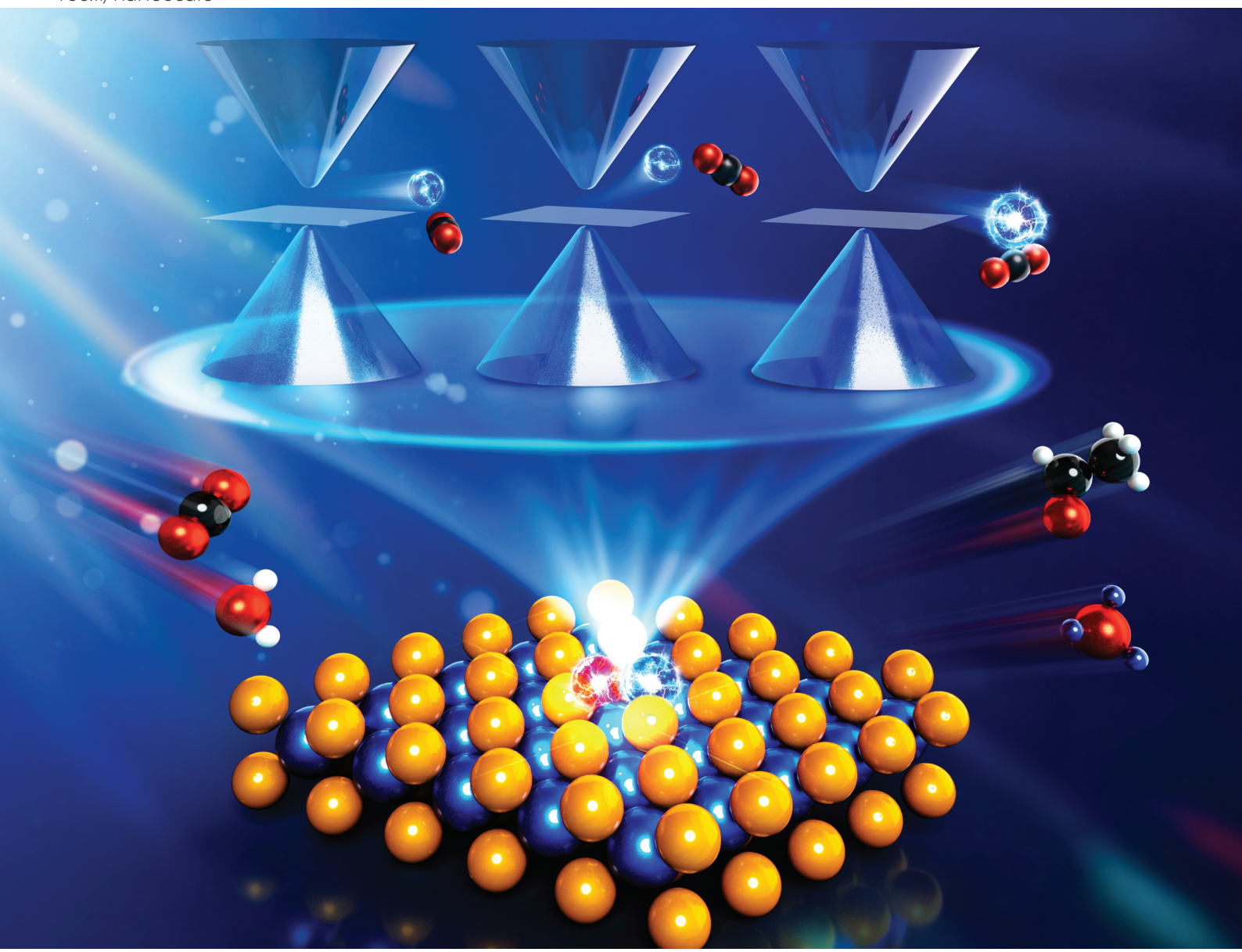

ISSN 2040-3372

ROYAL SOCIETY OF CHEMISTRY

PAPER

Yi-Fan Huang, Ruei-San Chen, Kuei-Hsien Chen, Li-Chyong Chen *et al.*

An *operando* photoconductivity platform reveals defect–adsorbate–carrier coupling in ultrathin MoS_2 for solar-driven CO_2 reduction

NCNST

Nanoscale

PAPER

View Article Online
View Journal | View Issue

Check for updates

Cite this: *Nanoscale*, 2025, **17**, 26698

An *operando* photoconductivity platform reveals defect–adsorbate–carrier coupling in ultrathin MoS_2 for solar-driven CO_2 reduction

Shang-Wei Ke,†[a,b] Chih-Yang Huang,†[a,c,d,e] Yi-Fan Huang,*[f] Yun-Hsuan Chan,[g] Ruei-San Chen,*[g] Kuei-Hsien Chen*[a,b,c] and Li-Chyong Chen*[a,h,i]

Understanding the interfacial charge dynamics between a catalyst and adsorbate is vital for advancing solar-driven CO_2 reduction. However, the mechanistic coupling between defects, surface adsorbates, and photogenerated carriers remains poorly defined under *operando* conditions, limiting rational catalyst design. Here, we introduce a high-sensitivity *in situ* photoconductivity (PC) platform to probe carrier dynamics in a 3 nm-thick MoS_2 film under simulated gas-phase CO_2 photoreduction conditions (AM1.5G illumination, CO_2/H_2O atmosphere). Prominent persistent PC (PPC) was observed under vacuum/UV irradiation, attributed to approximately 5% sulfur vacancies acting as deep-level traps (bandgap: 1.76 eV; electron capture barrier: 0.47 eV). Upon exposure to humid CO_2, the photocurrent dropped by 82%, with significantly shortened rise and decay time constants, indicating accelerated recombination *via* enhanced defect–adsorbate interactions. To explain these findings, we propose a conceptual defect–adsorbate energy alignment model describing three distinct electronic coupling scenarios, including (i) energetic alignment of defect–adsorbate states, (ii) modulation of adsorbate LUMO levels to higher energies, and (iii) lowering of adsorbate LUMO levels under specific coupling conditions. This model represents the first mechanistic framework linking adsorption, defect energetics, and charge retention in defective ultrathin 2D photocatalysts. It establishes a foundation for rational catalyst design, with future theoretical and spectroscopic validation expected to further strengthen this framework. Our *operando* PC platform offers mechanistic insights into defect–adsorbate–carrier coupling and provides a promising diagnostic tool for guiding the development of high-efficiency ultrathin 2D CO_2 catalysts.

Received 10th August 2025,
Accepted 30th September 2025

DOI: 10.1039/d5nr03394b

rsc.li/nanoscale

Open Access Article. Published on 27 oktobar 2025. Downloaded on 31.1.2026. 19.58.02.
This article is licensed under a Creative Commons Attribution-NonCommercial 3.0 Unported Licence.

1. Introduction

Carbon capture, utilization, and storage (CCUS) technologies are widely regarded as critical strategies for achieving net-zero carbon emissions.[1–3] Among the various CO_2 utilization approaches, solar-driven gas-phase photocatalytic CO_2 reduction reactions ($PCCO_2RRs$) offer a promising pathway for converting CO_2 into high-value fuels and chemicals using renewable energy sources.[4–6] However, traditional particulate photocatalysts such as metal oxides typically possess wide bandgaps, which limit light absorption and lead to long carrier diffusion paths and weak surface reactivity, consequently reducing overall catalytic performance.[7,8] In contrast, ultrathin two-dimensional (2D) semiconductor photocatalysts, such as molybdenum disulfide (MoS_2), have emerged as attractive alternatives due to their high surface-to-volume ratios, short charge migration lengths, and tunable electronic structures.[9–13] Their nanoscale thickness enhances charge separation and transport efficiency while reducing bulk recombination losses.[14,15] However, the full catalytic potential of these materials remains underexplored due to an incomplete understanding of how interfacial charge dynamics and gas-phase surface reactions co-evolve under realistic operating conditions.

[a]*Center for Condensed Matter Sciences, National Taiwan University, Taipei, 10617, Taiwan. E-mail: chenkh@pub.iams.sinica.edu.tw, chenlc@ntu.edu.tw*
[b]*Department of Chemistry, National Taiwan Normal University, Taipei, 11677, Taiwan*
[c]*Institute of Atomic and Molecular Sciences, Academia Sinica, Taipei, 10617, Taiwan*
[d]*International Graduate Program of Molecular Science and Technology, National Taiwan University (NTU-MST), Taipei 10617, Taiwan*
[e]*Molecular Science and Technology Program, Taiwan International Graduate Program (TIGP), Academia Sinica, Taipei 11529, Taiwan*
[f]*Department of Mechanical Engineering, National Chin Yi University of Technology, Taichung 41170, Taiwan. E-mail: yifanhuang@ncut.edu.tw*
[g]*Graduate Institute of Applied Science and Technology, National Taiwan University of Science and Technology, Taipei 10607, Taiwan. E-mail: rsc@mail.ntust.edu.tw*
[h]*Center of Atomic Initiative for New Materials, National Taiwan University, Taipei 10617, Taiwan*
[i]*Department of Physics, National Taiwan University, Taipei 10617, Taiwan*
†These authors contributed equally to this work.

This journal is © The Royal Society of Chemistry 2025

Open Access Article. Published on 27 oktobar 2025. Downloaded on 31.1.2026. 19.58.02.
This article is licensed under a Creative Commons Attribution-NonCommercial 3.0 Unported Licence.

Pristine MoS_2 was initially reported as an efficient HER catalyst because its edge sites are catalytically active,[16] whereas the basal plane is inert and unfavorable for catalytic reactions. However, the overall surface area of MoS_2 is dominated by the basal plane rather than the edge sites. If the basal plane properties can be effectively tuned, MoS_2 could potentially be transformed from an HER catalyst into a promising material for CO_2 reduction.[17] This possibility has attracted significant attention in recent years.[17–19] Strategies such as sulfur vacancy engineering and the introduction of supported metal single atoms or nanoparticles have been demonstrated to modify the electronic structure and catalytic behavior of the basal plane.[18,19] These approaches endow MoS_2 with remarkable potential for CO_2 conversion and have stimulated a new research direction.

Despite advances in the design and synthesis of 2D photocatalysts, the mechanistic coupling among intrinsic defects, adsorbed CO_2 molecules, and photogenerated charge carriers remains poorly understood under *operando* conditions.[20] A key mechanistic step involves the transfer of photogenerated electrons to adsorbed CO_2 molecules, which leads to the formation of $CO_2^{\bullet-}$, a crucial intermediate in the activation process.[8,21] The efficiency of this process depends not only on charge separation and transport but also on the energetic alignment and dynamic interaction between surface adsorbates and intrinsic defect states, which together modulate the interfacial charge landscape.[8,21] Intrinsic defects in ultrathin 2D photocatalysts, such as sulfur vacancies (V_S) or lattice distortions, substantially affect charge carrier behavior, enhance molecular adsorption, and regulate surface reaction pathways critical to photocatalytic CO_2 conversion.[22–24]

To evaluate catalytic performance, *ex situ* methods, such as gas chromatography (GC), gas chromatography–mass spectrometry (GC-MS), and nuclear magnetic resonance (NMR), are widely employed for product quantification,[25] yet these techniques provide no insight into real-time charge dynamics or surface–defect–adsorbate coupling. *In situ* spectroscopy, including X-ray photoelectron spectroscopy (XPS)[26,27] and diffuse reflectance infrared Fourier transform spectroscopy (DRIFTS),[28–30] enable chemical-state analysis of adsorbed species. However, these techniques primarily provide static snapshots of surface composition rather than dynamic information on charge behavior. Ultrafast transient absorption (TA) spectroscopy addresses this limitation by tracking carrier relaxation and trapping on the picosecond timescale and has been applied to study defect effects in $In_2O_{3-x}(OH)_y$ systems under photothermal CO_2/H_2 conditions.[30–32] However, TA is equipment intensive, and its ultrashort temporal window limits its applicability to steady-state processes such as persistent carrier retention or defect-mediated recombination, both of which are critical for determining photocatalytic turnover. These limitations expose a critical measurement gap: the lack of *operando*-compatible, steady-state electronic diagnostics capable of continuously resolving how surface–adsorbate interactions modulate charge retention *via* defect states. Without such tools, the role of defect–adsorbate–carrier coupling in regulating activation pathways and selectivity during the $PCCO_2RR$ remains speculative. Therefore, there is an urgent need for scalable, real-time diagnostic strategies that can directly probe photocarrier dynamics and their coupling with surface-adsorbed CO_2 under relevant gas-phase conditions, thus providing mechanistic guidance for rational defect engineering in ultrathin 2D photocatalysts.

Photoconductivity (PC) is a classical yet versatile optoelectronic technique that enables time-resolved monitoring of charge generation, transport, and recombination through systematic modulation of light intensity, wavelength, gas composition, and temperature under *operando* conditions.[33–35] Compared to conventional *ex situ* methods, PC is particularly well suited for probing carrier dynamics in low-dimensional semiconductors under reactive environments. PC measurements capture illumination-induced conductivity variations, serving as indirect but sensitive proxies for photocarrier generation efficiency, mobility, and trap-state dynamics. Numerous studies have reported varied photoconductivity (PC) responses in 2D materials, such as normal PC, persistent PC (PPC), and negative PC (NPC), which are commonly attributed to intrinsic defects and surface-adsorbed molecules.[34–37] PPC refers to a long-lived conductive state that persists even after illumination is removed, whereas NPC denotes a reduction in conductivity upon light exposure. Among these, PPC, defined as the prolonged conductivity after light-off, typically arises from deep-level trap states and may enhance multi-electron photocatalytic reactions by extending the lifetime of photogenerated electrons.[36,38] Despite its mechanistic significance, PPC remains largely underexplored in the context of dynamic defect–adsorbate–carrier coupling under photocatalytic conditions.

Our prior work extended *in situ* PC to gas-phase catalysis using carbon-doped SnS_2 under CO_2/H_2O, but PPC-specific behaviors were not systematically examined.[39] Notably, PPC has been reported in doped and nanostructured indium oxide systems, where defect-mediated trapping correlated with enhanced catalytic yields in gas-phase reverse water–gas shift (RWGS) reactions under $CO_2 + H_2$.[40,41] Their integration of *operando* PC characterization confirmed a positive correlation between PPC and catalytic performance. Although the RWGS system involves photothermal catalysis rather than pure photoexcited processes, its persistent photoconductivity behavior under illumination highlights the relevance of defect-assisted charge dynamics and supports the use of *operando* PC as a valuable mechanistic tool. To date, however, atomically thin 2D semiconductors have not yet been systematically evaluated for PPC behavior under realistic $PCCO_2RR$ conditions nor has the modulation of PPC *via* defect–adsorbate coupling been clarified. Furthermore, despite the growing number of review articles on *in situ* characterization techniques for photocatalysis,[29,30,42,43] *in situ* PC remains underutilized as a mechanistic probe, particularly in the case of PPC. Its capacity to resolve dynamic defect kinetics, long-lived charge retention, and interfacial electronic coupling under *operando* gas-phase conditions remains largely untapped. Addressing this knowledge gap is crucial for establishing a deeper mechanistic understanding of gas-phase photocatalysis and for developing scalable, material-agnostic PC diagnostics to screen PPC-active 2D catalysts and elucidate how defects influence CO_2 activation.

Open Access Article. Published on 27 oktobar 2025. Downloaded on 31.1.2026. 19.58.02.
This article is licensed under a Creative Commons Attribution-NonCommercial 3.0 Unported Licence.

To address the critical knowledge gap in defect–adsorbate–carrier coupling under gas-phase PCCO_2RR conditions, we developed a high-sensitivity *in situ* PC platform capable of real-time monitoring of charge dynamics in defective ultrathin 2D photocatalysts. Using a 3 nm-thick MoS_2 thin film (TF) as a model system, we observed pronounced PPC under vacuum/UV exposure, attributed to approximately 5% V_S acting as deep-level traps, consistent with a 1.76 eV optical bandgap and a 0.47 eV electron capture barrier (E_c) derived from Arrhenius and configuration coordinate analyses. Upon exposure to humid CO_2/AM1.5G illumination, the photocurrent decreased by 82%, while rise and decay time constants (τ_{rise} and τ_{fall}) were significantly shortened, indicating accelerated recombination and suppressed PPC *via* enhanced adsorbate-induced electron extraction. To rationalize these observations, we propose a conceptual defect–adsorbate energy alignment model that classifies three representative coupling scenarios based on the relative position of the CO_2 LUMO and defect trap states: (i) energetic alignment, (ii) higher LUMO, and (iii) lower LUMO. Although hypothetical, this model is substantiated by experimental observations and, to the best of our knowledge, represents the first mechanistic framework linking PPC modulation to defect–adsorbate electronic interactions in ultrathin 2D photocatalysts. Beyond offering mechanistic insights, our study positions *operando* PC as a generalizable diagnostic method for probing interfacial dynamics and guiding rational defect and surface energy design for solar-driven CO_2 photocatalysis.

2. Experimental methods

2.1 Preparation and characterization of 3 nm-thick MoS_2 thin films

Three-nanometer-thick MoS_2TFs were synthesized *via* post-sulfurization of vacuum-deposited 3 nm-thick molybdenum trioxide (MoO_3) TFs using a three-zone chemical vapor deposition (CVD) system, as illustrated in Fig. S1. High-purity sulfur (99.9%, Sigma-Aldrich) and MoO_3 powder (99.95%, Alfa Aesar) were used as precursor materials. The resulting MoS_2TFs grown on SiO_2/Si substrates were characterized using a suite of microscopy and spectroscopy techniques. Atomic force microscopy (AFM, Bruker Dimension Icon) was employed to determine the film thickness and surface roughness. Optical absorbance measurements were performed using a UV–vis–NIR spectrophotometer (JASCO V-670), and the optical band gap was estimated using Tauc plots derived from the absorbance spectra. Raman and photoluminescence (PL) spectra were acquired using a Jobin–Yvon LabRAM H800 system equipped with a 532 nm Nd:YAG laser as the excitation source. The chemical composition and stoichiometry of the MoS_2TF were analyzed *via* X-ray photoelectron spectroscopy (XPS, PHI 5000 VersaProbe III) using a monochromatic Al Kα source. The atomic sensitivity factors (ASFs) used for quantification were 3.544 for Mo 3d and 0.717 for S 2p, measured at a take-off angle of 54.7°. XPS data were processed and fitted using the CasaXPS software.

2.2 Dark/photocurrent and persistent photoconductivity

The photodetector structure based on the 3 nm-thick MoS_2 TF was designed in accordance with our previous studies,[35,39] adopting a two-terminal photoconductor configuration without gate bias. Platinum (Pt) top electrodes were deposited onto the MoS_2TF by sputtering. The ohmic behavior of the metal–semiconductor contact was verified using linear current–voltage (I–V) characteristics. All electrical measurements were carried out using a low-leakage current probe station (Lake Shore Cryotronics TTP4) integrated with a semiconductor characterization system (Keithley 4200-SCS). Dark and photocurrent responses were measured in vacuum at room temperature under illumination using three monochromatic light sources: a 375 nm ultraviolet (UV) laser, a 633 nm He–Ne laser, and an 808 nm diode laser. A constant DC bias of 1.0 V was applied during these measurements. To investigate PPC, the 3 nm-thick MoS_2TF sample was mounted on the cold finger of a closed-cycle helium cryostat, and PPC measurements were performed under 375 nm UV laser illumination at varying temperatures.

2.3 *In situ* photoconductivity measurements

In situ photoconductivity measurements were designed to probe the environmental sensitivity of the 3 nm-thick MoS_2TF device. Specifically, the photocurrent was measured in real-time while systematically varying the ambient conditions—from high vacuum ($\sim 1 \times 10^{-4}$ torr) to a mixed gas environment consisting of CO_2 and H_2O at 1 atm. These measurements were conducted under continuous AM1.5G simulated solar illumination and an applied bias of 1.0 V, as illustrated in Fig. S2. Additional experimental details related to the dark/photocurrent, *in situ* photocurrent, and PPC characterization are available in our previous reports.[35,36,39]

2.4 Photocatalytic CO_2 reduction measurement

A 3 nm-thick MoS_2TF was evaluated for its photocatalytic CO_2 reduction performance under a 24-hour illumination period. The gaseous products generated from the PC-CO_2RR process were analyzed using a gas chromatography system (Agilent 6890) equipped with a flame ionization detector (FID) and a glass PLOT column (RT-Q-BOND). This analytical configuration enabled reliable separation and quantification of the reaction products. Further information regarding the GC system setup and reaction conditions can be found in our earlier publications.[44]

3. Results and discussion

3.1 Conceptual design of the *in situ* photocurrent platform for gas-phase CO_2 photocatalysis

To systematically investigate charge transport and photocarrier retention in ultrathin 2D photocatalysts under solar-driven

 This journal is © The Royal Society of Chemistry 2025

Open Access Article. Published on 27 oktobar 2025. Downloaded on 31.1.2026. 19.58.02.
This article is licensed under a Creative Commons Attribution-NonCommercial 3.0 Unported Licence.

gas-phase $PCCO_2RR$ conditions, we developed a high-sensitivity *in situ* photoconductivity platform capable of real-time electrical probing under simulated solar illumination and controlled atmospheres (Fig. 1). As shown in Fig. 1a, ultrathin MoS_2TF was selected as a model photocatalyst due to its atomically thin structure, strong light–matter interaction, and the presence of intrinsic defects characteristic of 2D MoS_2, making it a promising system for real-time mechanistic studies.

To achieve this, we established an experimental configuration that combines steady-state AM1.5G illumination with a gas-phase reactor enabling exposure to reactive $CO_2 + H_2O$ mixtures. The planar photodetector architecture (Fig. 1b) allows for direct and continuous photocurrent monitoring without the need for a gate electrode, enabling real-time tracking of charge transport while the catalyst interacts with surface adsorbates. A constant bias voltage of 1.0 V was applied during all measurements to maintain stable current collection. This configuration provides not only real-time conductivity measurements but also establishes a mechanistic foundation for correlating dynamic electrical responses with interfacial gas–solid processes. In particular, it enables time-resolved tracking of PPC modulation and interfacial electron extraction, both of which are critical for elucidating the coupling between photogenerated carriers, intrinsic defect states, and surface-adsorbed species. Such *operando*-compatible diagnosis is essential for deciphering the mechanistic basis of defect–adsorbate–carrier interactions in ultrathin 2D photocatalysts for solar-driven CO_2 reduction. The material characteristics and defect properties of the ultrathin MoS_2TF used in this study are described in the following section.

3.2 Fabrication and multimodal characterization of 3 nm MoS_2 photocatalytic films

The 3 nm-thick MoS_2TFs were synthesized by post-sulfurization of 3 nm-thick MoO_3 TF, following our previously established method.[44,45] Initially, MoO_3 TFs were deposited onto SiO_2/Si substrates by thermal evaporation. These were then annealed at 500 °C for 1 hour under an Ar–H_2 (4 : 1) atmosphere at ~1 Torr to convert MoO_3 into MoO_2. Post-sulfurization was conducted under Ar–H_2 (10 : 1) at 1 Torr, with sulfur powder heated to 140 °C and the substrate heated to 900 °C. After 10 minutes of reaction, MoO_3 was fully converted into MoS_2 (Fig. S1). The resulting 3 nm-thick MoS_2TF grown on SiO_2/Si substrates is shown in Fig. 2a. Optical microscopy and AFM confirmed the formation of a continuous, large-area film (Fig. 2b and c). The film thickness was measured to be approximately 3.0 nm, and the root-mean-square surface roughness (R_q) was 0.48 nm, determined *via* AFM height profiling on a scratched region (Fig. 2c). These results demonstrate the successful fabrication of uniform ultrathin films with smooth surfaces suitable for electronic measurements.

Raman spectroscopy verified the 2H-MoS_2 phase, revealing two characteristic peaks corresponding to the in-plane (E^1_{2g}, 382.8 cm^{-1}) and out-of-plane (A_{1g}, 407.5 cm^{-1}) vibrational modes of Mo–S bonding (Fig. 2d). The Si substrate peak appeared at ~521 cm^{-1}. To further assess spatial uniformity, Raman spectra were collected from 16 positions across a 2 × 1 cm^2 area. The frequency difference between the A_{1g} and E^1_{2g} modes remained consistent at ~24.7 cm^{-1}, indicating excellent thickness homogeneity (Fig. 2e). For comparison, spectra from commercial monolayer and bulk MoS_2 crystals were also included. Optical absorption properties were analyzed using UV–vis–NIR spectroscopy (Fig. 2f). Three distinct excitonic features were observed at 669, 618, and 444 nm, corresponding to the A, B, and C excitons, respectively. The inset of Fig. 2f shows a Tauc plot estimating the optical band gap at ~1.76 eV. Temperature-dependent photoluminescence (PL) spectra were recorded over the 550–800 nm range (Fig. 2g), displaying A and B exciton emissions. PL intensity increased with decreasing temperature from room temperature to 80 K, indicating reduced non-radiative recombination.

XPS was used to analyze the chemical composition and stoichiometry of the MoS_2TF. High-resolution spectra of the Mo 3d and S 2p regions are shown in Fig. 2h and i, respectively. The Mo 3d spectrum displayed two main peaks at 229.4 eV ($3d_{5/2}$) and 232.5 eV ($3d_{3/2}$), along with a small S 2s peak at 226.6 eV (Fig. 2h).[46,47] The S 2p spectrum exhibited a doublet at 162.2 eV ($2p_{3/2}$) and 163.4 eV ($2p_{1/2}$), characteristic of Mo–S

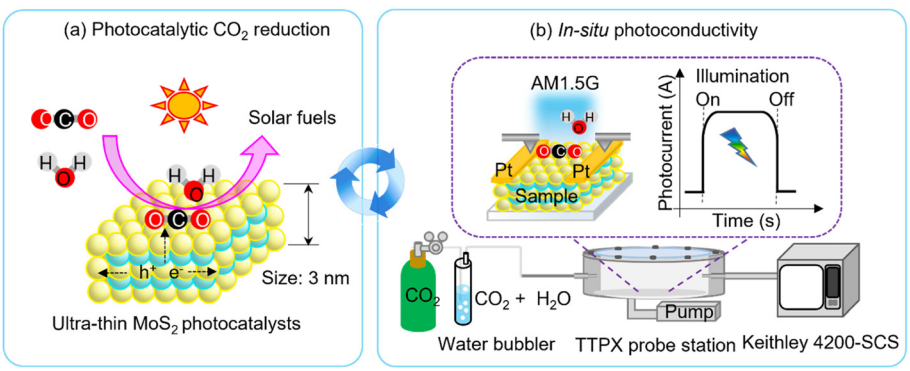

Fig. 1 (a) Schematic illustration of a 3 nm-thick MoS_2TF serving as a model photocatalyst for the solar-driven $PCCO_2RR$. (b) A planar MoS_2TF-based photodetector architecture for *in situ* photocurrent measurement, enabling real-time electrical probing of carrier dynamics and defect–adsorbate interactions under the solar-driven gas-phase $PCCO_2RR$.

Open Access Article. Published on 27 oktobar 2025. Downloaded on 31.1.2026. 19.58.02.
This article is licensed under a Creative Commons Attribution-NonCommercial 3.0 Unported Licence.

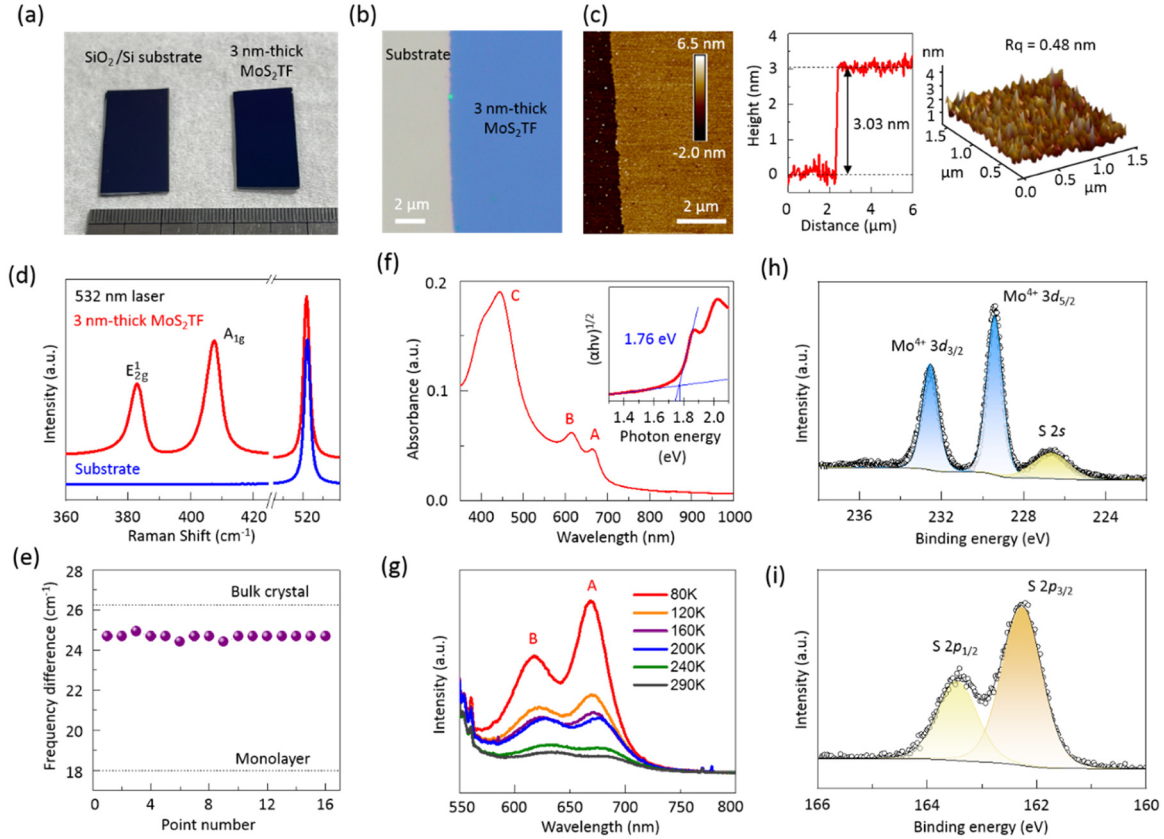

Fig. 2 (a) Photographs of the SiO_2/Si substrates before (left) and after (right) the growth of the 3 nm-thick MoS_2TF. (b) Optical microscopy image and (c) atomic force microscopy (AFM) images of the as-grown 3 nm-thick MoS_2TF, including surface height profiles and surface roughness characterization on the SiO_2/Si substrate. (d) Raman spectra of the 3 nm-thick MoS_2TF and the bare SiO_2/Si substrate, recorded using a 532 nm excitation laser. (e) Statistical distribution of the frequency difference between the A_{1g} and E^1_{2g} Raman modes obtained from 16 different points on the 3 nm-thick MoS_2TF. Distributions from commercial monolayer and bulk MoS_2 crystals are included for comparison. (f) UV–vis–NIR absorption spectrum and (g) temperature-dependent photoluminescence (PL) spectra of the 3 nm-thick MoS_2TF. The inset in (f) shows the Tauc plot used to estimate the optical band gap. (h and i) High-resolution XPS spectra of the Mo 3d (h) and S 2p (i) core-level regions for the 3 nm-thick MoS_2TF on the SiO_2/Si substrate.

bonding (Fig. 2i).[46–48] Quantitative XPS analysis yielded an S : Mo atomic ratio of 1.9, suggesting the presence of ~5% V_S in the film. The complete XPS survey spectrum is presented in Fig. S3. Overall, this comprehensive characterization confirmed the successful synthesis of ultrathin MoS_2TF with controlled thickness, uniform morphology, and well-defined chemical composition. These attributes are essential prerequisites for subsequent investigations of their intrinsic photoconductive properties and photocatalytic behavior.

3.3 Intrinsic photoconductivity of 3 nm-thick MoS_2TF

3.3.1 Wavelength- and power-dependent photoconductivity behavior. The intrinsic photoconductive properties of the 3 nm-thick MoS_2TF were systematically investigated under vacuum at room temperature. The experimental setup is shown in Fig. S2a. All current–voltage and time-resolved measurements were conducted with a constant bias voltage of 1.0 V. Linear and symmetric *I–V* curves confirmed good ohmic contact with the platinum electrodes in both vacuum and CO_2 + H_2O gas environments (Fig. S2b). Fig. 3 shows the wavelength-dependent photocurrent responses under three laser excitations operating at the same power (375, 633, and 808 nm, 20 mW). The light was modulated in 10-minute on/off cycles over three repetitions, and signals were baseline-corrected by subtracting the dark current (Fig. 3a–c). The photocurrent magnitude strongly depended on excitation wavelength: UV illumination (375 nm) yielded the highest response (~8 nA), followed by 633 nm (~1.9 nA) and 808 nm (~0.7 nA) (Fig. 3d). This trend is consistent with the absorption spectrum shown in Fig. 2f, in which stronger absorption results in higher photocurrent generation. Additionally, power-dependent measurements under 633 nm illumination (20–40 mW) confirmed that photocurrent increased proportionally with laser power (Fig. S4). Notably, only 375 nm excitation induced a PPC effect, characterized by a slow decay of the photocurrent after the light was turned off, as discussed in detail in section 3.3.2.

3.3.2 Persistent photoconductivity behavior in ultrathin MoS_2TF. Temperature-dependent photocurrent measurements were conducted to further examine PPC (Fig. 4). In this study,

 This journal is © The Royal Society of Chemistry 2025

Open Access Article. Published on 27 oktobar 2025. Downloaded on 31.1.2026. 19.58.02.
This article is licensed under a Creative Commons Attribution-NonCommercial 3.0 Unported Licence.

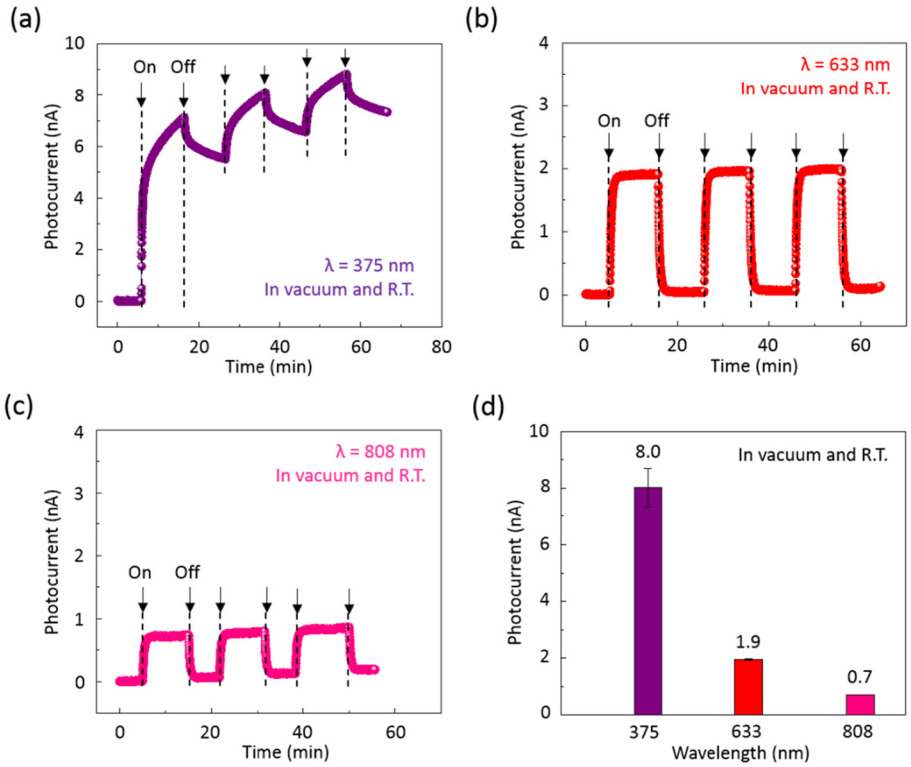

Fig. 3 Wavelength-dependent photocurrent response of the 3 nm-thick MoS_2TF under vacuum and room temperature conditions. Time-resolved photocurrent measurements were performed under laser illumination at 20 mW for three different wavelengths: (a) 375 nm (UV), (b) 633 nm (visible), and (c) 808 nm (near-infrared). (d) Averaged steady-state photocurrent values of the 3 nm-thick MoS_2TF under each wavelength, with dark current subtracted.

the PPC analysis followed established protocols for investigating defect-related conductivity and metastable carrier trapping in wide-bandgap semiconductors.[36,49] As shown in Fig. 4a, at 150 K under 375 nm illumination and vacuum conditions, the photocurrent increased by nearly one order of magnitude and remained elevated for over 26 minutes after light-off. To assess thermal stability, a three-step temperature cycle was performed (Fig. 4b): cooling from 330 K to 150 K (current decreased), illumination at 150 K (current rose rapidly), and reheating to 330 K (current gradually returned toward the baseline). These measurements illustrate the persistence of photoexcited carriers and the metastable trapping states involved. Normalized decay curves measured at various temperatures are shown in Fig. 4c. Each curve was fitted using a stretched exponential function:[50]

$$I(t) = I_{(0)}\exp[-(t/\tau)^{\beta}], 0 < \beta < 1, \quad (1)$$

where τ is the decay time constant and β is the stretch exponent. The extracted β values (0.33–0.16) indicate a broad distribution of relaxation pathways, consistent with large lattice relaxation models.[51] To quantify the thermal activation energy for carrier recapture, the temperature dependence of τ was evaluated using an Arrhenius relation:

$$\tau \propto \exp(E_c/kT), \quad (2)$$

where E_c denotes the electron capture barrier. As shown in Fig. 4d, two regimes were observed: τ decreased rapidly at higher temperatures, indicating thermally activated capture, while τ remained nearly constant at low temperatures, consistent with tunneling-assisted recombination. From the high-temperature slope, E_c was determined to be approximately 0.47 eV. This energy barrier represents the threshold required for electrons to return from the conduction band to defect states, providing a mechanistic explanation for the prolonged carrier lifetimes observed in PPC.

Finally, the configuration coordinate diagram in Fig. 4e illustrates the transition between stable deep-level states and metastable shallow donor states, offering a physical framework for interpreting the long-lived photocurrent decay. Collectively, these findings highlight that PPC in ultrathin MoS_2TF arises from defect-related metastable states, which can significantly influence charge separation and recombination processes relevant to photocatalysis.

3.4 Real-time probing of catalytic activity and PPC dynamics in ultrathin MoS_2TF

3.4.1 Photocatalytic CO_2 reduction performance. Gas-phase CO_2 photoreduction experiments were performed under simulated solar irradiation for 24 hours, with a blank control for comparison (section 2.4). As shown in Fig. 5a, the 3 nm-

Open Access Article. Published on 27 oktobar 2025. Downloaded on 31.1.2026. 19.58.02.
This article is licensed under a Creative Commons Attribution-NonCommercial 3.0 Unported Licence.

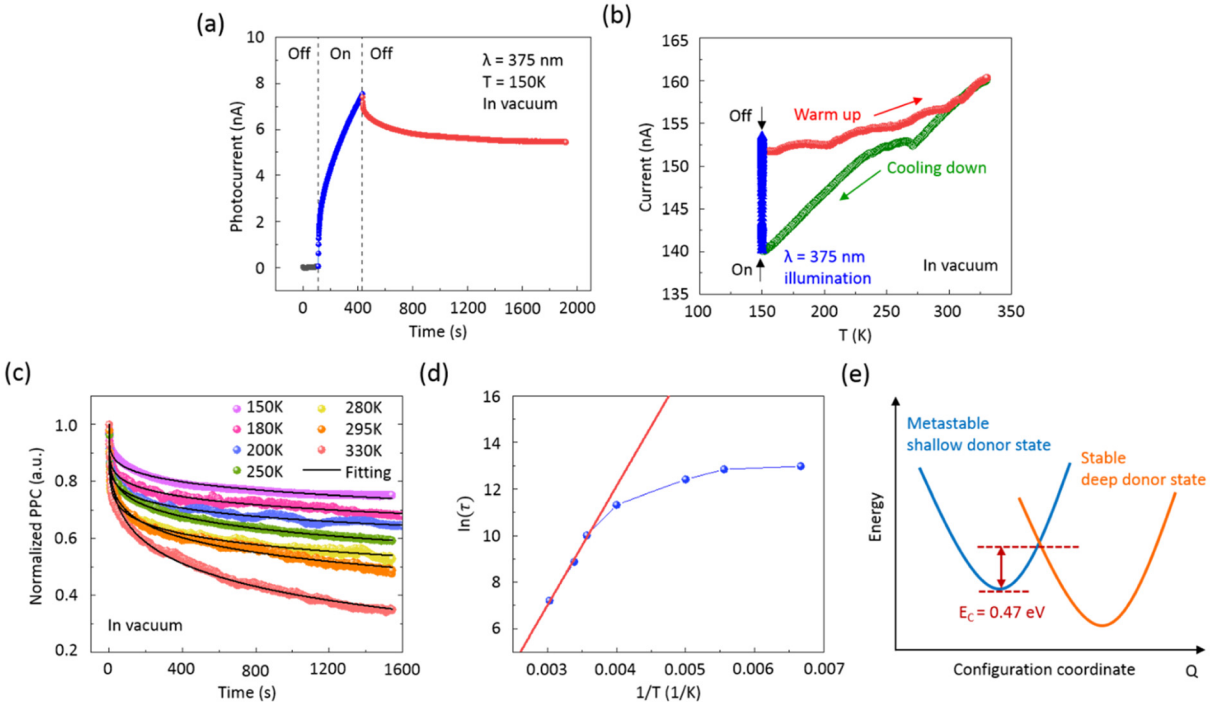

Fig. 4 Temperature-dependent PPC behavior and configuration coordinate analysis of 3 nm-thick MoS_2TF. (a) Representative PPC buildup and decay response of 3 nm-thick MoS_2TF measured at 150 K under vacuum. (b) Temperature-dependent current response of 3 nm-thick MoS_2TF before, during, and after illumination with a 375 nm laser. (c) Normalized PPC decay curves of 3 nm-thick MoS_2TF collected at different temperatures. Dark current was subtracted from all measurements. (d) Arrhenius plot of the PPC decay time constant ($\ln\tau$ *versus* $1/T$) for 3 nm-thick MoS_2TF. Blue spheres represent experimental data and the red line corresponds to the fit based on eqn (2). (e) Schematic configuration coordinate diagram illustrating the transition between a metastable shallow donor state (blue parabola curve) and a stable deep donor state (orange parabola curve) in 3 nm-thick MoS_2TF. E_c represents the electron capture barrier energy.

thick MoS_2TF produced methane (CH_4) and acetaldehyde (CH_3CHO), with a total yield of 431 nmol m^{-2}. Isotopic $^{13}CO_2$ reduction experiments further confirmed that CH_4 exhibited a complete ^{13}C signal, and the CH_3 fragment of CH_3CHO showed ^{13}C labeling, verifying their assignment as genuine CO_2 photoreduction products (Fig. S5). Although CH_3CHO exhibited only partial ^{13}C incorporation ($^{13}CH_3$ + ^{12}CHO), the detection of a labeled CH_3 fragment clearly indicates that it is at least partially derived from CO_2 reduction. While film-based photocatalyst yields are typically lower than those of powder materials,[52,53] ultrathin planar architectures offer advantages for mechanistic studies by providing well-defined interfaces and controllable defect environments. This work presents the first demonstration of gas-phase CO_2 photoreduction using an ultrathin 3 nm MoS_2TF, enabling direct correlation between catalytic output and charge dynamics. To uncover the underlying photoelectronic behavior, *in situ* photoconductivity measurements were carried out under the same reaction conditions, offering time-resolved insight into carrier dynamics and PPC modulation. Although the photocatalytic CO_2RR experiments yielded a mixture of products, reflecting the long-standing selectivity challenge of MoS_2-based systems, the primary focus of this work is to establish mechanistic insights using *operando* photoconductivity rather than to optimize product selectivity. According to previous reports, surface modification strategies (*e.g.*, sulfur vacancy engineering and supported Au single atoms or nanoparticles) have proved effective in enhancing product selectivity in MoS_2 catalysts.[18,19] These approaches represent promising directions for future studies aiming to improve the CO_2RR performance. With these considerations in mind, we next examine the *in situ* photocurrent response under identical CO_2RR conditions to correlate catalytic outputs with the underlying charge dynamics.

3.4.2 *In situ* photocurrent response under CO_2 reduction conditions. *In situ* photocurrent measurements were conducted to further examine the behavior of the 3 nm-thick MoS_2TF under conditions relevant to solar-driven CO_2 reduction (Fig. 5b). Experiments alternated between vacuum and humid CO_2 (CO_2 + H_2O) environments under AM1.5G illumination and a constant applied bias of 1 V. Under vacuum, the device exhibited a clear PPC behaviour (blue curve in the lower panel of Fig. 5b), characterized by a rapid initial rise in photocurrent followed by a slower increase, eventually reaching ~39.7 nA after 10 minutes of illumination. After the light was switched off, the photocurrent decayed gradually and remained at ~15.8 nA after 30 minutes in darkness. In contrast, under humid CO_2 (red curve in the lower panel of Fig. 5b), the photocurrent reached ~7 nA during illumination

 This journal is © The Royal Society of Chemistry 2025

Open Access Article. Published on 27 oktobar 2025. Downloaded on 31.1.2026. 19.58.02.
This article is licensed under a Creative Commons Attribution-NonCommercial 3.0 Unported Licence.

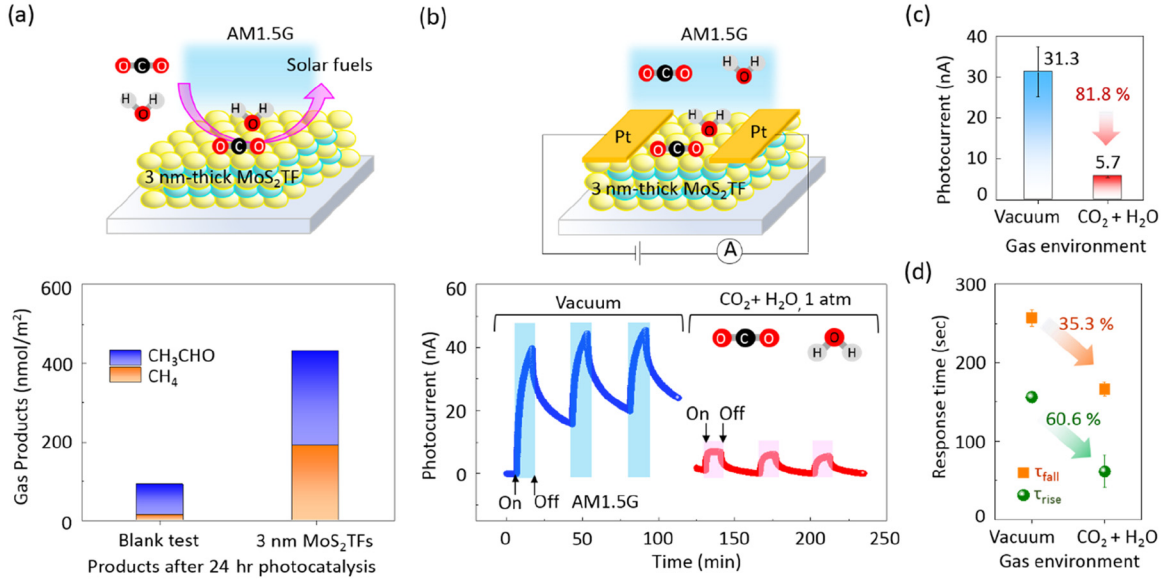

Fig. 5 Photocatalytic performance and *in situ* photocurrent response of the 3 nm-thick MoS_2TF. (a) Schematic illustration (top) of solar-driven photocatalytic CO_2 reduction using the 3 nm-thick MoS_2TF and the corresponding gaseous products (bottom) generated after 24 hours of reaction. The total gaseous products include CH_4, CH_3CHO, C_2H_4, and C_3H_6O. (b) Schematic diagram (top) of the *in situ* photoconductivity measurement platform, and the corresponding time-resolved photocurrent responses (bottom) of the 3 nm-thick MoS_2TF under two gas environments: vacuum (blue) and CO_2 + H_2O (red). (c) Comparison of the average photocurrent and (d) photoresponse time constants (τ_{rise} and τ_{fall}) under vacuum and CO_2 + H_2O conditions. All measurements were performed under AM1.5G simulated sunlight. Photocurrent values were corrected by subtracting the baseline dark current.

and decayed rapidly to ~1 nA after the light was turned off, indicating strong suppression of PPC due to gas-phase interactions.

Fig. 5c quantifies these differences more systematically. The average photocurrent over three illumination cycles decreased from 31.3 nA in vacuum to 5.7 nA in humid CO_2, corresponding to an ~82% reduction in signal amplitude. Fig. 5d presents the extracted rise and decay time constants (τ_{rise} and τ_{fall}) under both environments. In vacuum, τ_{rise} and τ_{fall} were measured as 156 s and 275 s, respectively. Under humid CO_2, they decreased to 61 s and 167 s. These values were obtained by fitting the time-resolved photocurrent transients to exponential decay functions (details in Fig. S6). Notably, τ_{rise} decreased by ~60%, while τ_{fall} decreased by ~35%, highlighting that humid CO_2 not only reduced photocurrent amplitude but also accelerated the temporal evolution of recombination dynamics. From a photocatalytic perspective, this decrease in photocurrent should not be regarded solely as a loss of conductivity. Rather, it reflects enhanced electron extraction by surface-adsorbed CO_2/H_2O species, indicating that photogenerated carriers are being actively utilized in CO_2 activation processes. Although the measurable signal is reduced, the observed behavior provides direct evidence that electrons are diverted away from the conductive pathway and utilized in CO_2 photoreduction reactions. To disentangle the spectral contribution to PPC, control measurements using a 633 nm laser were performed. These experiments confirmed that PPC was induced by the UV component of the AM1.5G spectrum. No PPC behavior was observed under 633 nm illumination in either gas environment (Fig. S7).

To better understand the mechanistic implications of these observations, it is instructive to consider the physical processes associated with τ_{rise} and τ_{fall}. During illumination, electron–hole pairs are generated in the MoS_2TF. These carriers must be separated and transported to contribute to the photocurrent. The rise time constant (τ_{rise}) reflects the time required for carriers to transition from generation to formation of a steady conduction pathway. A shorter τ_{rise} indicates faster carrier extraction. Under humid CO_2, τ_{rise} decreased by ~60%, suggesting that adsorbed CO_2 molecules may facilitate faster carrier transfer *via* additional surface channels or transient trapping sites. When illumination is turned off, carriers recombine or are captured by defect states. The decay constant (τ_{fall}) reflects carrier recombination or trapping dynamics, with shorter values indicating faster loss pathways. Under humid CO_2, τ_{fall} was ~35% shorter, indicating accelerated decay of the photocurrent, likely due to enhanced electron capture by adsorbed CO_2 species acting as recombination centers. Overall, these findings demonstrate that humid CO_2 exerts a dual influence: it accelerates initial carrier extraction and transport (shorter τ_{rise}) but also promotes faster recombination (shorter τ_{fall}). From a photocatalytic perspective, this dual effect may facilitate electron transfer to adsorbed reactants but could also shorten carrier lifetimes, potentially limiting overall efficiency. Such dual modulation of charge dynamics implies that surface adsorbates may influence defect-state occupancy

Open Access Article. Published on 27 oktobar 2025. Downloaded on 31.1.2026. 19.58.02.
This article is licensed under a Creative Commons Attribution-NonCommercial 3.0 Unported Licence.

or depth, thereby shifting the energy landscape of photocarrier retention. These results clearly demonstrate the dynamic modulation of photocarrier behavior by surface adsorbates, reflecting a complex interplay between charge transport and recombination processes at defect-rich ultrathin interfaces. The observed shortening of τ_{rise} and τ_{fall}, along with the suppressed PPC, suggests that adsorbate-induced perturbations may influence the energetics of defect states. These observations motivate the energy-level coupling model presented in section 3.6, where defect–adsorbate–carrier interactions are explicitly rationalized to account for the observed PPC modulation and recombination kinetics.

Importantly, to the best of our knowledge, this study represents the first experimental observation of PPC in an ultrathin MoS_2TF under simulated solar-driven CO_2 reduction conditions. While prior PPC reports in MoS_2 were largely limited to field-effect transistor configurations under vacuum or inert environments,[54–59] our results extend this understanding to *operando* gas-phase photocatalytic systems, highlighting the pivotal role of surface adsorbates in modulating defect-state energetics and photocarrier retention. This observation not only demonstrates the functional relevance of PPC in catalytically active conditions but also provides a mechanistic basis for the energy-level alignment model presented in section 3.5, where the coupling between intrinsic defects, surface adsorbates, and photocarriers is explicitly rationalized.

3.5 Photoconductivity-based mechanistic elucidation and energy-level model of defect–adsorbate–carrier coupling

In this study, we systematically employed an *in situ* photoconductivity platform to probe the microscopic interactions among intrinsic defects, surface adsorbates, and photogenerated carriers in ultrathin MoS_2 photocatalysts under simulated gas-phase $PCCO_2RR$ conditions. This platform resolves real-time processes such as CO_2 activation, carrier generation, transport, trapping, and recombination, enabling a mechanistic foundation for rational defect engineering in 2D materials. To construct this framework, we highlight three mechanistic pillars: (i) the correlation between specific defect structures and photoconductivity behaviors; (ii) the dual modulation of charge dynamics by CO_2 adsorption; (iii) an energy-level alignment model describing how defect–adsorbate coupling governs PPC.

(i) Photoconductivity behavior serves as a sensitive indicator of defect–carrier coupling. As illustrated in Fig. 6a, four representative defect types,[22,60] namely 0D vacancies or dopants, 1D dislocations, 2D grain boundaries, and 3D heterogeneities, can serve as catalytic sites that facilitate CO_2 adsorption and activation. However, the corresponding photoconductive responses, including normal PC, PPC, and NPC, have not yet been systematically classified (Fig. 6b). In our study, a 3 nm MoS_2 thin film containing ~5% V_S exhibited pronounced PPC under $PCCO_2RR$ conditions. Previous spectroscopic and DFT studies have shown that V_S in MoS_2 introduce localized states below the conduction band edge.[61] These divergences across prior studies suggest that photoconductivity behavior is highly sensitive to both defect configuration and environmental gas composition. We suggest that *in situ* photoconductivity can serve as a high-throughput diagnostic tool for screening the defect–gas interactions under catalytic conditions.

(ii) Adsorbed CO_2 molecules simultaneously influence carrier extraction and recombination. Based on our measurements under humid CO_2 conditions, the photoconductivity rise and decay time constants (τ_{rise} and τ_{fall}) were shortened by approximately 60% and 35%, respectively, accompanied by a substantial decrease in steady-state PPC (Fig. 5b–d). These findings indicate that CO_2 dynamically modulates trap occupancy by interacting with defect states at the catalyst surface. Fig. 6b schematically illustrates three representative photoconductivity behaviors (Type I: PC, Type II: PPC, and Type III: NPC), each exhibiting distinct rise and decay time constants. Although only the PPC case was directly observed in our experiment, we infer that the physical parameters governing photoconductivity dynamics, such as carrier retention and recombination rates, are likely influenced by gas-phase conditions across all three types. This implies a broader research opportunity to systematically study how $PCCO_2RR$ environments modulate photoconductivity in different defect configurations. Fig. 6c further bridges the photoelectronic response to molecular events, depicting CO_2 photoactivation *via* electron injection into its LUMO ($2\pi_u$), forming bent $CO_2^{\bullet-}$ intermediates.[8,21] Although this classic mechanism does not explicitly include defects, we expand it by proposing that adsorbate–defect coupling alters interfacial charge transfer and carrier lifetimes through energy-level interaction.

(iii) To interpret the role of defects in modulating PPC, we propose a conceptual energy-level alignment model (Fig. 6d), which relates the LUMO energy level of adsorbed CO_2 to the energetic position of defect-induced trap states. The model considers three representative alignment scenarios. In Scenario I, the CO_2 LUMO is energetically aligned with the trap states introduced by V_S, enabling efficient electron transfer from the defect to the adsorbate and thereby depleting trapped carriers, which leads to suppression of PPC. In Scenario II, the CO_2 LUMO lies above the defect level, resulting in unfavorable electron injection and prolonged carrier trapping, thus sustaining the PPC effect. In Scenario III, the LUMO of CO_2 resides below the defect energy level, allowing rapid extraction of electrons from the traps and consequently causing an abrupt quenching of PPC. This alignment-based interpretation provides a new perspective on how sulfur-vacancy-derived trap states modulate photoconductivity *via* interaction with adsorbed molecules. Although the model remains conceptual, further validation through density functional theory (DFT) simulations or band-alignment measurements such as XPS and ultraviolet photoelectron spectroscopy (UPS) is warranted to quantitatively assess the proposed scenarios, towards a coherent framework linking defect energetics with gas-phase carrier dynamics. Such DFT and XPS/UPS studies are beyond the scope of this study.

 This journal is © The Royal Society of Chemistry 2025

Open Access Article. Published on 27 oktobar 2025. Downloaded on 31.1.2026. 19.58.02.
This article is licensed under a Creative Commons Attribution-NonCommercial 3.0 Unported Licence.

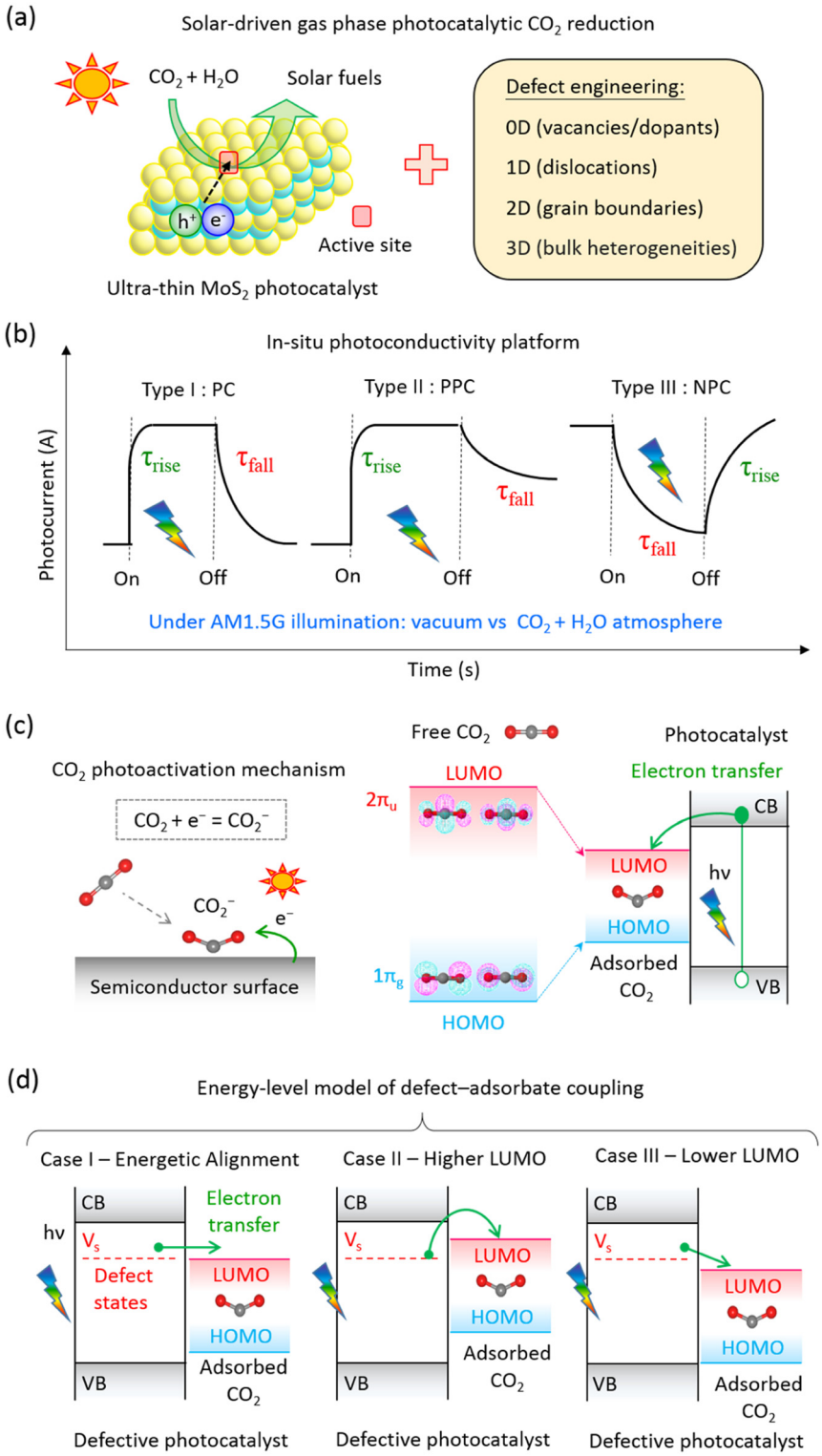

Fig. 6 Mechanistic framework of defect–adsorbate–carrier coupling in ultrathin MoS_2TF for solar-driven CO_2 reduction. (a) Schematic of gas-phase CO_2 photoreduction using defect-engineered ultrathin MoS_2TF, highlighting four catalytic defect classes: 0D (vacancies/dopants), 1D (dislocations), 2D (grain boundaries), and 3D (bulk heterogeneities). (b) An *in situ* photoconductivity platform for classifying MoS_2 photoconductivity under PCCO$_2$RR conditions (AM1.5G + CO_2/H_2O), enabling identification of Type I (PC), Type II (PPC), and Type III (NPC) behaviors, along with analysis of photocurrent and response times (τ_{rise} and τ_{fall}). (c) CO_2 photoactivation mechanism, where photogenerated electrons are injected into the CO_2 LUMO ($2\pi_u$), generating bent $CO_2^{\bullet-}$ intermediates and triggering redox reactions. (d) Proposed energy-level alignment model based on sulfur vacancies (V_S), illustrating how defect–adsorbate coupling modulates PPC: Scenario I – aligned energy levels promote electron transfer, quenching PPC; Scenario II – higher LUMO prevents transfer, sustaining PPC; Scenario III – lower LUMO rapidly extracts electrons, leading to rapid PPC decay. This model provides a mechanistic foundation for understanding defect–adsorbate–carrier interactions and guiding photocatalyst design.

Open Access Article. Published on 27 oktobar 2025. Downloaded on 31.1.2026. 19.58.02.
This article is licensed under a Creative Commons Attribution-NonCommercial 3.0 Unported Licence.

To our knowledge, this is the first mechanistic model that directly links defect–adsorbate–carrier coupling to measurable PPC behavior in ultrathin 2D photocatalysts under solar-driven CO_2 reduction. Such insights may guide future defect engineering strategies aimed at optimizing carrier lifetimes and interfacial reactivity. This platform could also be extended to explore how tailored defect densities, surface chemistries, and band alignments affect photocatalyst performance.

4. Conclusions

In this study, we developed a high-sensitivity *operando* PC platform to investigate persistent photoconductivity (PPC) in ultrathin MoS_2TF under simulated solar-driven CO_2 photoreduction conditions. Our results revealed that sulfur vacancies (~5%) act as deep-level traps that drive PPC under vacuum/UV light conditions, evidenced by a 1.76 eV bandgap and 0.47 eV electron capture barrier. Under humid CO_2, an 82% drop in photocurrent and shortened rise/decay constants indicated enhanced charge extraction by adsorbates, leading to PPC suppression. To rationalize these observations, we proposed a hypothetical energy-level alignment model that conceptually links defect states with the electronic structure of adsorbed CO_2. This represents the first *operando* mechanistic demonstration of PPC regulation in 2D photocatalysts during gas-phase CO_2 activation. Beyond providing mechanistic insight, our *operando* PC strategy offers a scalable diagnostic and rational design basis for defect-engineered screening and optimization of next-generation solar-driven CO_2 reduction catalysts. Future integration of *in situ* PC with theoretical modeling or XPS/UPS measurements may further validate this framework and unlock defect-specific design rules for predictive catalyst development.

Author contributions

Shang-Wei Ke: investigation, data curation, and formal analysis. Chih-Yang Huang: investigation, data curation, and formal analysis. Yi-Fan Huang: conceptualization, investigation, data curation, formal analysis, writing – original draft, writing – review & editing, and supervision. Yun-Hsuan Chan: data curation. Ruei-San Chen: resources, funding acquisition, and supervision. Kuei-Hsien Chen: resources, funding acquisition and supervision. Li-Chyong Chen: resources, funding acquisition, writing – original draft, writing – review & editing, and supervision.

Conflicts of interest

There are no conflicts to declare.

Data availability

The data supporting this article are included in the supplementary information (SI). Supplementary information is available. See DOI: https://doi.org/10.1039/d5nr03394b.

Additional information is available from the corresponding authors upon reasonable request.

Acknowledgements

This study was supported by the Ministry of Science and Technology (MOST), Taiwan (Grant No. 111-2112-M-011-004-MY3 and GG14840501C4), and by the National Science and Technology Council (NSTC), Taiwan (Grant No. 112-2622-E-011-007, 114-2113-M-001-006, 112-2639-M-002-005-ASP and 113-2639-M-002-004-ASP). Additional financial support from the Center of Atomic Initiative for New Materials, National Taiwan University, from the Featured Areas Research Center Program within the framework of the Higher Education Sprout Project by the Ministry of Education in Taiwan (112L9008 and 113L9008) is also acknowledged. Y. F. H. gratefully acknowledges additional support from the IAMS Junior Fellowship, Institute of Atomic and Molecular Sciences, Academia Sinica.

References

1 S. Chu and A. Majumdar, *Nature*, 2012, **488**, 294–303.
2 J. C. Abanades, E. S. Rubin, M. Mazzotti and H. J. Herzog, *Energy Environ. Sci.*, 2017, **10**, 2491–2499.
3 S. J. Davis, N. S. Lewis, M. Shaner, S. Aggarwal, D. Arent, I. L. Azevedo, S. M. Benson, T. Bradley, J. Brouwer, Y.-M. Chiang, C. T. M. Clark, A. Cohen, S. Doig, J. Edmonds, P. Fennell, C. B. Field, B. Hannegan, B. M. Hodge, M. I. Heffert, E. Ingersoll, P. Jaramillo, K. S. Lackner, K. J. Mach, M. Mastrandrea, J. Ogden, P. F. Peterson, D. L. Sanchaz, D. Sperling, J. Stagner, J. E. Trancik, C. J. Yang and K. Caldeira, *Science*, 2018, **360**, eaas9793.
4 O. S. Bushuyev, P. De Luna, C. T. Dinh, L. Tao, G. Saur, J. van de Lagemaat, S. O. Kelley and E. H. Sargent, *Joule*, 2018, **2**, 825–832.
5 E. V. Kondratenko, G. Mul, J. Baltrusaitis, G. O. Larrazábal and J. Pérez-Ramírez, *Energy Environ. Sci.*, 2013, **6**, 3112–3135.
6 S. Fang, M. Rahaman, J. Bharti, E. Reisner, M. Robert, G. A. Ozin and Y. H. Hu, *Nat. Rev. Methods Primers*, 2023, **3**, 61.
7 V. P. Indrakanti, J. D. Kubicki and H. H. Schobert, *Energy Environ. Sci.*, 2009, **2**, 745–758.
8 X. Chang, T. Wang and J. Gong, *Energy Environ. Sci.*, 2016, **9**, 2177–2196.
9 H. Wang, X. Zhang and Y. Xie, *Mater. Sci. Eng., R*, 2018, **130**, 1–39.
10 S. Hu and M. Zhu, *ChemCatChem*, 2019, **11**, 6147–6165.
11 X. Yang, D. Singh and R. Ahuja, *Catalysts*, 2020, **10**, 1111.

 This journal is © The Royal Society of Chemistry 2025

Open Access Article. Published on 27 oktobar 2025. Downloaded on 31.1.2026. 19.58.02.
This article is licensed under a Creative Commons Attribution-NonCommercial 3.0 Unported Licence.

12 C. Lai, N. An, B. Li, M. Zhang, H. Yi, S. Liu, L. Qin, X. Liu, L. Li, Y. Fu, F. Xu, Z. Wang, X. Shi, Z. An and X. Zhou, *Chem. Eng. J.*, 2021, **406**, 126780.
13 M. Li, H. Zhang, Z. Zhao, P. Wang, Y. Li and S. Zhan, *Acc. Mater. Res.*, 2023, **4**, 4–15.
14 J. Xiong, J. Di and H. Li, *J. Mater. Chem. A*, 2020, **8**, 12928–12950.
15 F. Chen, T. Ma, T. Zhang, Y. Zhang and H. Huang, *Adv. Mater.*, 2021, **33**, 2005256.
16 T. F. Jaramillo, K. P. Jørgensen, J. Bonde, J. H. Nielsen, S. Horch and I. Chorkendorff, *Science*, 2007, **317**, 100–102.
17 Z. Meng, J. Fan, A. Chen and X. Xie, *Mater. Today Chem.*, 2023, **29**, 101449.
18 J. Hu, L. Yu, J. Deng, Y. Wang, K. Cheng, C. Ma, Q. Zhang, W. Wen, S. Yu, Y. Pan, J. Yang, H. Ma, F. Qi, Y. Wang, Y. Zheng, M. Chen, R. Huang, S. Zhang, Z. Zhao, J. Mao, X. Meng, Q. Ji, G. Hou, X. Han, X. Bao, Y. Wang and D. Deng, *Nat. Catal.*, 2021, **4**, 242–250.
19 C. Chen, C. Ye, X. Zhao, Y. Zhang, R. Li, Q. Zhang, H. Zhang and Y. Wu, *Nat. Commun.*, 2024, **15**, 7825.
20 R. Yanagi, T. Zhao, D. Solanki, Z. Pan and S. Hu, *ACS Energy Lett.*, 2021, **7**, 432–452.
21 A. Álvarez, M. Borges, J. Corral-Pérez, J. Olcina, L. Hu, D. Cornu, R. Huang, D. Stoian and A. Urakawa, *ChemPhysChem*, 2017, **18**, 3135–3141.
22 S. Bai, N. Zhang, C. Gao and Y. Xiong, *Nano Energy*, 2018, **53**, 296–336.
23 J. Di, G. Hao, W. Jiang and Z. Liu, *Acc. Mater. Res.*, 2023, **4**, 910–924.
24 Y. Ma, B. Qiu, J. Zhang and M. Xing, *ChemNanoMat*, 2021, **7**, 368–379.
25 M. Bonchio, J. Bonin, O. Ishitani, T. B. Lu, T. Morikawa, A. J. Morris, E. Reisner, D. Sarkar, F. M. Toma and M. Robert, *Nat. Catal.*, 2023, **6**, 657–665.
26 M. Salmeron and R. Schlögl, *Surf. Sci. Rep.*, 2008, **63**, 169–199.
27 M. Favaro, H. Xiao, T. Cheng, W. A. Goddard III, J. Yano and E. J. Crumlin, *Proc. Natl. Acad. Sci. U. S. A.*, 2017, **114**, 6706–6711.
28 S. S. Bhosale, A. K. Kharade, S. Narra, S. M. Chang and E. Wei-Guang Diau, *ACS Energy Lett.*, 2023, **8**, 280–288.
29 C. Mu, C. Lv, X. Meng, J. Sun, Z. Tong and K. Huang, *Adv. Mater. Interfaces*, 2023, **10**, 2201842.
30 H. Issa Hamoud, L. Wolski, I. Pankin, M. A. Bañares, M. Daturi and M. El-Roz, *Top. Curr. Chem.*, 2022, **380**, 37.
31 N. Li, Y. Ma and W. Sun, *Molecules*, 2024, **29**, 3995.
32 L. B. Hoch, P. Szymanski, K. K. Ghuman, L. He, K. Liao, Q. Qiao, L. M. Reyes, Y. Zhu, M. A. El-Sayed, C. V. Singh and G. A. Ozin, *Proc. Natl. Acad. Sci. U. S. A.*, 2016, **113**, E8011–E8020.
33 *Photoconductivity: art: science & technology*, ed. N. V. Joshi, CRC Press, 1990.
34 C. J. Docherty, C. T. Lin, H. J. Joyce, R. J. Nicholas, L. M. Herz, L. J. Li and M. B. Johnston, *Nat. Commun.*, 2012, **3**, 1228.
35 W. C. Shen, R. S. Chen and Y. S. Huang, *Nanoscale Res. Lett.*, 2016, **11**, 1–7.
36 Y. C. Lee, J. L. Shen, K. W. Chen, W. Z. Lee, S. Y. Hu, K. K. Tiong and Y. S. Huang, *J. Appl. Phys.*, 2006, **99**, 063706.
37 X. Xiao, J. Li, J. Wu, D. Lu and C. Tang, *Appl. Phys. A*, 2019, **125**, 1–7.
38 S. L. Gao, L. P. Qiu, J. Zhang, W. P. Han, S. Ramakrishna and Y. Z. Long, *ACS Appl. Electron. Mater.*, 2024, **6**, 1542–1561.
39 T. Billo, I. Shown, A. k. Anbalagan, T. A. Effendi, A. Sabbah, F. Y. Fu, C. M. Chu, W. Y. Woon, R. S. Chen, C. H. Lee, K. H. Chen and L. C. Chen, *Nano Energy*, 2020, **72**, 104717.
40 J. Y. Loh, A. Mohan, A. G. Flood, G. A. Ozin and N. P. Kherani, *Nat. Commun.*, 2021, **12**, 402.
41 J. Y. Loh, M. Shayegannia and N. P. Kherani, *Appl. Catal., B*, 2021, **282**, 119555.
42 Z. Fang, Y. Liu, C. Song, P. Tao, W. Shang, T. Deng, X. Zeng and J. Wu, *J. Semicond.*, 2022, **43**, 041104.
43 M. Hu, J. Alharbi, H. Zhang, H. S. Al Qahtani and C. Feng, *Chem. Res. Chin. Univ.*, 2025, **41**, 237–253.
44 Y. F. Huang, K. W. Liao, F. R. Z. Fahmi, V. A. Modak, S. H. Tsai, S. W. Ke, C. H. Wang, L. C. Chen and K. H. Chen, *Catalysts*, 2021, **11**, 1295.
45 Y. K. Lin, R. S. Chen, T. C. Chou, Y. H. Lee, Y. F. Chen, K. H. Chen and L. C. Chen, *ACS Appl. Mater. Interfaces*, 2016, **8**, 22637–22646.
46 H. Vrubel and X. Hu, *ACS Catal.*, 2013, **3**, 2002–2011.
47 D. Ganta, S. Sinha and R. T. Haasch, *Surf. Sci. Spectra*, 2014, **21**, 19.
48 C. C. Cheng, A. Y. Lu, C. C. Tseng, X. Yang, M. N. Hedhili, M. C. Chen, K. H. Wei and L. J. Li, *Nano Energy*, 2016, **30**, 846–852.
49 J. Z. Li, J. Y. Lin, H. X. Jiang, A. Salvador, A. Botchkarev and H. Morkoc, *Appl. Phys. Lett.*, 1996, **69**, 1474–1476.
50 J. Y. Lin, A. Dissanayake, G. Brown and H. X. Jiang, *Phys. Rev. B:Condens. Matter Mater. Phys.*, 1990, **42**, 5855.
51 D. V. Lang and R. A. Logan, *Phys. Rev. Lett.*, 1977, **39**, 635.
52 I. Shown, S. Samireddi, Y. C. Chang, R. Putikam, P. H. Chang, A. Sabbah, F. Y. Fu, W. F. Chen, C. I. Wu, T. Y. Yu, P. W. Chung, M. C. Lin, L. C. Chen and K. H. Chen, *Nat. Commun.*, 2018, **9**, 169.
53 Y. Zhang, B. Xia, J. Ran, K. Davey and S. Z. Qiao, *Adv. Energy Mater.*, 2020, **10**, 1903879.
54 Y. C. Wu, C. H. Liu, S. Y. Chen, F. Y. Shih, P. H. Ho, C. W. Chen, C. T. Liang and W. H. Wang, *Sci. Rep.*, 2015, **5**, 11472.
55 N. Rathi, S. Rathi, I. Lee, J. Wang, M. Kang, D. Lim, M. A. Khan, Y. Lee and G. H. Kim, *RSC Adv.*, 2016, **6**, 23961–23967.
56 A. Di Bartolomeo, L. Genovese, T. Foller, F. Giubileo, G. Luongo, L. Croin, S. J. Liang, L. Ang and M. Schleberger, *Nanotechnology*, 2017, **28**, 214002.
57 A. George, M. V. Fistul, M. Gruenewald, D. Kaiser, T. Lehnert, R. Mupparapu, C. Neumann, U. Hübner, M. Schaal, N. Masurkar, L. M. R. Arava, I. Staude,

Open Access Article. Published on 27 oktobar 2025. Downloaded on 31.1.2026. 19.58.02.
This article is licensed under a Creative Commons Attribution-NonCommercial 3.0 Unported Licence.

U. Kaiser, T. Fritz and A. Turchanin, *npj 2D Mater. Appl.*, 2021, **5**, 15.
58 C. Chandan, S. Sarkar and B. Angadi, *Appl. Phys. Lett.*, 2021, **118**, 172105.
59 P. H. Ci, X. Z. Tian, J. Kang, A. Salazar, K. Eriguchi, S. Warkander, K. C. Tang, J. M. Liu, Y. B. Chen, S. Tongay, W. Walukiewicz, J. W. Miao, O. Dubon and J. Q. Wu, *Nat. Commun.*, 2020, **11**, 5373.
60 P. Muhammad, A. Zada, J. Rashid, S. Hanif, Y. Gao, C. Li, Y. Li, K. Fan and Y. Wang, *Adv. Funct. Mater.*, 2024, **34**, 2314686.
61 M. H. Naik and M. Jain, *Phys. Rev. Mater.*, 2018, **2**, 084002.

This journal is © The Royal Society of Chemistry 2025